ACS Photonics

Article

Cite This: ACS Photonics 2019, 6, 211−220

pubs.acs.org/journal/apchd5

# Completely Spin-Decoupled Dual-Phase Hybrid Metasurfaces for Arbitrary Wavefront Control

He-Xiu Xu,[*,†,‡,#] Lei Han,[‡,§,#] Ying Li,[‡] Yunming Sun,[∥] Jianlin Zhao,[§] Shuang Zhang,[⊥] and Cheng-Wei Qiu[*,‡]

[†]Air and Missile Defense College, Air Force Engineering University, Xi'an 710051, China

[‡]Department of Electrical and Computer Engineering, National University of Singapore, Singapore 117583, Singapore

[§]MOE Key Laboratory of Material Physics and Chemistry under Extraordinary Conditions, Shaanxi Key Laboratory of Optical Information Technology, School of Natural and Applied Sciences, Northwestern Polytechnical University, Xi'an 710072, China

[∥]Advanced Technique Department, Key Lab of Aeronautics Computing Technique, Xi'an 710175, China

[⊥]School of Physics & Astronomy, University of Birmingham, Birmingham B15 2TT, U.K.

Supporting Information



**ABSTRACT:** Controlling light with a thin flat device is highly desirable in modern optics. A particular prospect in this area is a metasurface that independently shows distinct functionalities for different kinds of incoming waves. However, to date this is mostly achieved on anisotropic metasurfaces based on different propagation phases under two orthogonal linear polarizations. On the other hand, achieving multifunctionality for the two circularly polarized (CP) waves is very important in view of the growing significance of spin photonics. However, achieving completely decoupled optical functions for different photon spins is very challenging and remains elusive. Available attempts were only confined to locked spin-flipped phase profile to achieve opposite vortex modes, converged/diverged focusing, and interchanged holographic images. Here, we propose a general strategy to break this limitation by involving hybrid *geometric* and *propagation* phases with extremely low polarization cross-talk (an order of magnitude suppression). We experimentally demonstrate our scheme with two versatile CP bifunctional devices operating at microwaves. Besides, the possible applications have been illustrated from the perspective of stealth and information entropy by imposing dual irregular phase patterns in two completely decoupled helicity channels. The finding in this study is expected to trigger great interest in electromagnetic/optical integration and complex electromagnetic wave manipulations with a new degree of freedom.

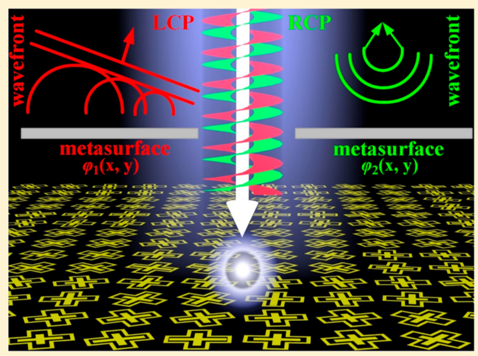


**KEYWORDS:** *anisotropic metasurface, helicity control, bifunctional devices, polarization cross-talk, geometric phase*

Independent wavefront control integrated into one single plate under two arbitrary orthogonal polarization states is crucial in modern science and technology since it meets the increasing demands of high speed/capacity of flat electromagnetic (EM) and optical devices. Anisotropic metasurfaces, subwavelength-spaced linearly birefringent phase-shifters, have attracted much attention due to their superior capabilities of EM wavefront control under different polarizations.[1−10] Unfortunately, these metasurfaces with structural anisotropy and parametric variations (propagation phase) only work under two orthogonal linear polarization (LP) states, which poses severe limitations on practical applications. Recently, Pancharatnam−Berry (PB) metasurfaces based on the geometric phase have been utilized to realize helicity- or wavelength-multiplexed metalenses and holograms under left-handed and right-handed circularly polarized (LCP and RCP) waves.[11−22] Although desired functionalities can be realized based on the incident/detected combination of LCP/RCP waves, the functionalities under LCP and RCP waves are essentially locked together due to the opposite phase profile flipping as the spin state of incident waves. Such a monotonic functionality poses great limitations and hinders practical applications.[16,17] Therefore, the previous helicity multiplexing approach still cannot accomplish the task of independent wave control at two orthogonal states of circularly polarized (CP) waves, and encoding simultaneously two types of geometric phase profiles onto the metasurface may complicate the design.

Most recently, complete phase and polarization control was achieved by combining both the geometric and propagation phases[23−25] (termed the hybrid method hereafter). Therein, the independent wave control can be engineered at arbitrary orthogonal states of polarization even including at two elliptical waves in the optical region. Such a strategy affords an unprecedented degree of freedom in modulating the wavefront of EM waves. However, the ideal phase decoupling between any

**Received:** October 16, 2018
**Published:** December 3, 2018




DOI: 10.1021/acsphotonics.8b01439
ACS Photonics 2019, 6, 211−220

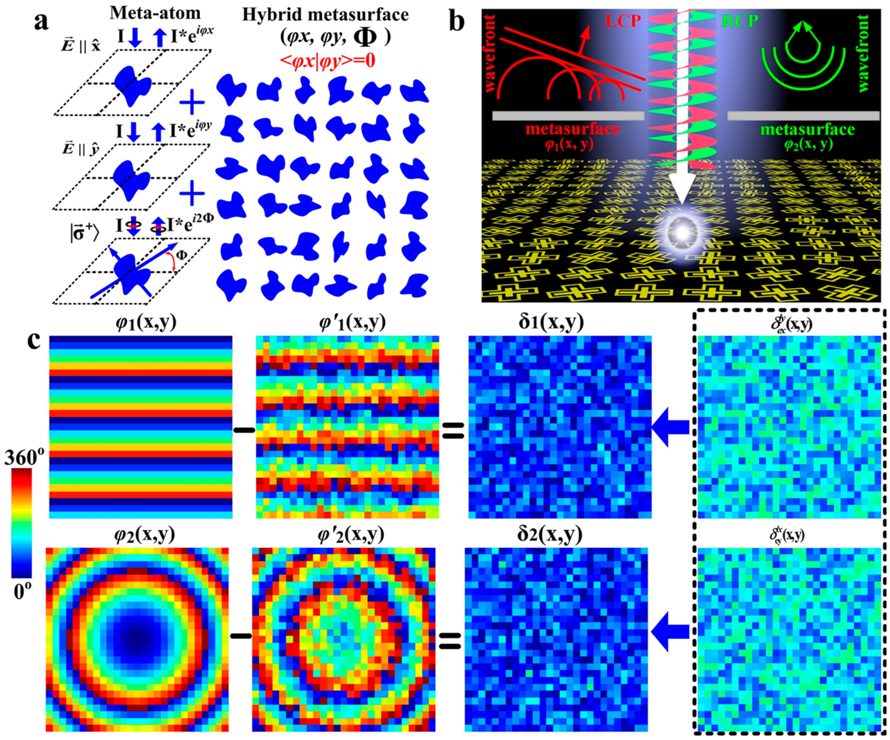


**Figure 1.** Conceptual illustration of design processes and independent wavefront control using our spin-decoupled metasurface. (a) Three types of phases (left panel) to design our metasurfaces consisting of spatially rotated and structurally varied conceptual meta-atoms with arbitrary irregular inclusions (right panel). Here, $\langle\varphi_x|\varphi_y\rangle = 0$ represents the ideal case with no LP cross-talk. (b) Illustration of two completely different wavefronts, i.e., an oblique planar wavefront and a focusing wavefront. (c) Theoretically calculated phase distortions $\delta_1$ and $\delta_2$ to $\varphi_1$ and $\varphi_2$ caused by LP cross-talk $\delta_{ex}^{ly}$ and $\delta_{ey}^{lx}$ typically exhibited in conventional meta-atoms made of metallic rectangular-patch or elliptical-pillar patterns on a dielectric-spaced metal ground.

two orthogonal polarization states is challenging due to the strong polarization cross-talk of available meta-atoms in practice. This is especially true for the rectangular-patch and pillar meta-atom (discussed below) realized at microwave frequencies using normal low-index substrates, where the LP cross-talk is very considerable. We find such an LP cross-talk contributes to the distortions of CP phases and thus sacrifices the efficiency of the resultant spin-dependent multiplexing devices. Otherwise, a dual parametric scanning process over two structural variations along orthogonal LP directions is necessary, which prohibitively enhances the computation volume (exponential growth) and complicates the design. Up to now, engineering extremely low LP cross-talk to realize completely spin-decoupled dual distinct CP functionalities in the microwave region is rarely reported.

In this study, we advance the hybrid method in a general case by considering cross-talk commonly available in practice and propose a method for a completely spin-decoupled dual-phase metasurface with a distortion-free CP phase profile and then report for the first time high-efficiency wavefront control under two orthogonal spin states at microwave frequencies. The utilized meta-atoms feature extremely low LP cross-talk, which guarantees high-efficiency and precise CP operation. As a proof of concept, we experimentally realize two bifunctional metadevices: one simultaneously possessing distinct functionalities of beam bending and focusing, and the other capable of generating multiple highly directive beams and a diffraction-free Bessel beam, respectively, for the two spin states. As an illustration of application, two irregular phase patterns are merged into dual completely decoupled helicity channels from the perspective of stealth and information entropy. Our approach represents a simpler but highly efficient strategy to achieve real spin-driven flat multifunctional metadevices, complementary to previous propagation-phase-based polarization switchable devices.[1−10]

## RESULTS

**Fundamentals and Theory for Completely Decoupled Helicity Modulation.** Cross-talk is a long-held but very tricky topic, especially in the closely spaced highly integrated channels where unshielded electromagnetic signals interfere with each other. Phase cross-talk at two arbitrary orthogonal LP waves is very universal and strongly undesirable in bifunctional birefringent spatial wave modulation. The common feature of a meta-atom exhibiting low LP cross-talk is that the structural variations along one polarization do not alter the phase response at the other. Without losing generality, for an arbitrary anisotropic metasurface under the Cartesian coordinate system, we need eight variables ($\xi_{ex}^{lx}(\sigma)$, $\xi_{ex}^{ly}(\sigma)$, $\xi_{ey}^{lx}(\sigma)$, and $\xi_{ey}^{ly}(\sigma)$; $\sigma = x$ or $y$ denotes the gradient directions) to fully describe (design) the two-dimensional (2D) phase gradients under two orthogonal structure orientations and polarizations.

$$\begin{bmatrix} \xi_{ex}^{lx}(\sigma) & \xi_{ex}^{ly}(\sigma) \\ \xi_{ey}^{lx}(\sigma) & \xi_{ey}^{ly}(\sigma) \end{bmatrix} = \begin{bmatrix} \dfrac{\partial\varphi_{ex}^{lx}(x, y)}{\partial\sigma} & \dfrac{\partial\varphi_{ex}^{ly}(x, y)}{\partial\sigma} \\ \dfrac{\partial\varphi_{ey}^{lx}(x, y)}{\partial\sigma} & \dfrac{\partial\varphi_{ey}^{ly}(x, y)}{\partial\sigma} \end{bmatrix} \tag{1}$$

Here, *ex* and *ey* represent the linear polarization states and *lx* and *ly* refer to parametric variations along the *x* and *y* directions, respectively. $\varphi_{ex}^{lx}$ and $\varphi_{ex}^{ly}$ describe the acquired propagation


DOI: 10.1021/acsphotonics.8b01439
ACS Photonics 2019, 6, 211−220

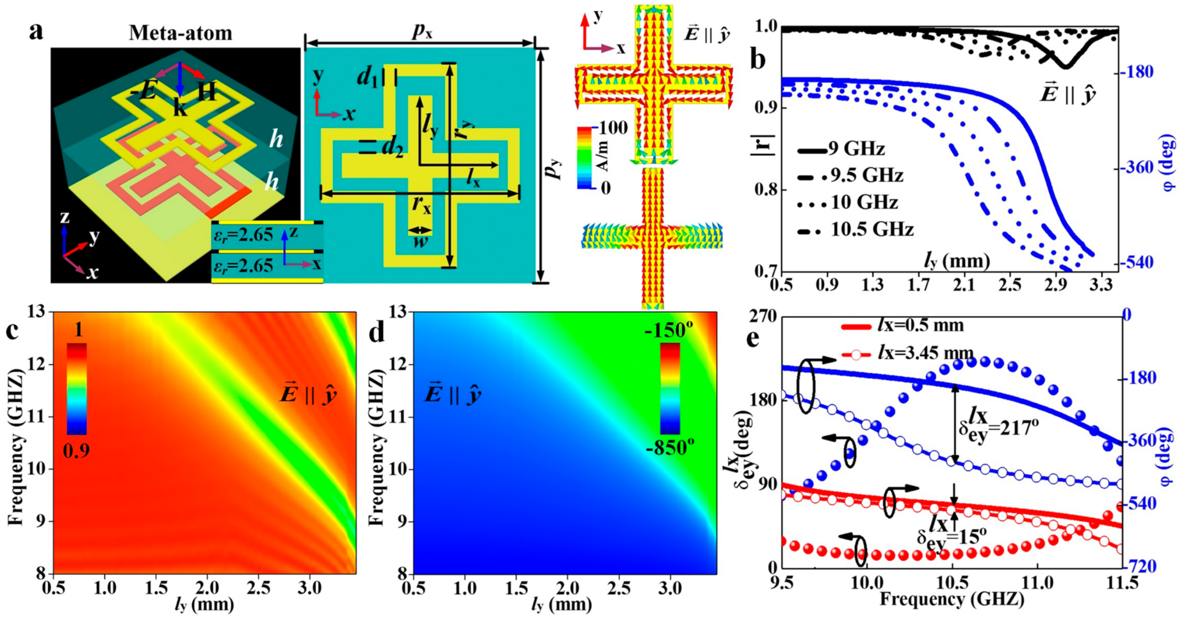


**Figure 2.** Characterization of the designed anisotropic dual-layered meta-atom with low LP cross-talk. (a) Topology of the meta-atoms using composite cross bar and cross loop. The right panel shows the current distributions on the top metallic patterns with (top) and without (bottom) the cross loop at 9.9 GHz. (b) Reflection spectra of the meta-atom as a function of *ly* under *y* polarization at different frequencies of 9, 9.5, 10, and 10.5 GHz. Reflection (c) magnitude and (d) phase of the meta-atom in a 2D color map versus frequency and *ly*. (e) FDTD-simulated LP cross-talk measured by $\delta^{lx}_{ey} = \varphi^{lx}_{ey}(lx_{\min}) - \varphi^{lx}_{ey}(lx_{\max})$ for the previous rectangular-patch or elliptical-pillar (blue color) and proposed meta-atoms (red color) when $l_x$ varies from 0.5 to 3.45 mm while keeping other parameters constant. Here, the meta-atoms with rectangular-patch and elliptical-pillar metallic patterns on backed metallic ground manifest similar LP cross-talk issues. The residual geometrical parameters are $p_x = p_y = 9.5$ mm, $r_x = r_y = 8.1$ mm, $d_1 = d_2 = 0.5$ mm, and $w = 1$ mm. In (b), $l_x = 2$ mm, while in (e) $l_y = 3.45$ mm.

phases through *x*- and *y*-oriented structural variations under *x* polarization, whereas $\varphi^{lx}_{ey}$ and $\varphi^{ly}_{ey}$ represent the imposed propagation phases under *y* polarization. For ideal anisotropic metasurfaces without LP cross-talk, $\varphi^{ly}_{ex}$ and $\varphi^{lx}_{ey}$ should remain a constant, and thus $\xi^{ly}_{ex}(\sigma) = \xi^{lx}_{ey}(\sigma) = 0$. However, cross-talk always exists and $\varphi^{ly}_{ex}$ and $\varphi^{lx}_{ey}$ cannot be constant in practice. Such an effect imparts phase distortions to the $\varphi^{lx}_{ex}$ and $\varphi^{ly}_{ey}$ through additional perturbation phases $\delta^{ly}_{ex}$ and $\delta^{lx}_{ey}$, which are functions of $\varphi^{ly}_{ex}$ and $\varphi^{lx}_{ey}$, respectively, and a measure of LP cross-talk. In the following, we show that such an LP phase cross-talk counter-intuitively contributes to the distortion of the CP phase profile.

The spin-decoupled design starts from a general case at an arbitrary polarization state, where the output components are related to the input ones through Jones matrix; see Supporting Information. By adopting the specific dual CP phases of $\varphi_1(x, y)$ and $\varphi_2(x, y)$ for distinct bifunctionalities in this work, the Jones matrix can be immediately derived as

$$\boldsymbol{J}(x, y) = \begin{bmatrix} e^{i\varphi_1(x,y)} & e^{i\varphi_2(x,y)} \\ -ie^{i\varphi_1(x,y)} & ie^{i\varphi_2(x,y)} \end{bmatrix} \begin{bmatrix} 1 & 1 \\ i & -i \end{bmatrix}^{-1} \tag{2}$$

On the other hand, any symmetric and unitary Jones matrix can be described as a function of its eigenvalue $\varphi_x$ and $\varphi_y$ and orientation angle of the meta-atom Φ:[23,24]

$$\boldsymbol{J}(x, y) = \boldsymbol{R}(-\Phi) \begin{bmatrix} e^{i\varphi_x} & 0 \\ 0 & e^{i\varphi_y} \end{bmatrix} \boldsymbol{R}(\Phi) \tag{3}$$

with $\boldsymbol{R}(\Phi) = \begin{bmatrix} \cos\Phi & \sin\Phi \\ -\sin\Phi & \cos\Phi \end{bmatrix}$ Here, $\varphi_x$ and $\varphi_y$ are propagation phases under CP wave excitation corresponding to aforementioned $\varphi^{lx}_{ex}$ and $\varphi^{ly}_{ey}$ in the LP case without cross-talk, and Φ is related to half of the geometric phase. By substituting eq 3 into eq 2 and a projection of $\varphi_1(x, y)$ and $\varphi_2(x, y)$, we can derive individually $\varphi_x$, $\varphi_y$, and Φ shown in Figure 1a to engineer arbitrary CP wavefront control. Therefore, the spin-decoupled design typically consists of three steps, as conceptually depicted in Figure 1a. First, one needs to design $\varphi_1(x, y)$ and $\varphi_2(x, y)$ according to two predefined distinct functionalities shown in Figure 1b; then one can calculate $\varphi_x$, $\varphi_y$, and Φ; finally one can design a set of meta-atoms with spatially varied structures (*lx* and *ly*) and orientations to form a metasurface (see left panel in Figure 1a). A CAD (computer-aided design) is established which can automatically implement all the above procedures through program codes in a commercial software. However, LP cross-talk is inevitable in practice, and therefore eq 3 should be rewritten as


DOI: 10.1021/acsphotonics.8b01439
ACS Photonics 2019, 6, 211−220

$$\boldsymbol{J}(x, y) = \boldsymbol{R}(-\Phi)\begin{bmatrix} e^{i(\varphi_{ex}^{lx}+\delta_{ex}^{ly})} & 0 \\ 0 & e^{i(\varphi_{ey}^{ly}+\delta_{ey}^{lx})} \end{bmatrix}\boldsymbol{R}(\Phi)$$
$$= \begin{bmatrix} e^{i(\varphi_{ex}^{lx}+\delta_{ex}^{ly})}\cos^2\Phi + e^{i(\varphi_{ey}^{ly}+\delta_{ey}^{lx})}\sin^2\Phi & \frac{1}{2}\sin 2\Phi(e^{i(\varphi_{ex}^{lx}+\delta_{ex}^{ly})} - e^{i(\varphi_{ey}^{ly}+\delta_{ey}^{lx})}) \\ \frac{1}{2}\sin 2\Phi(e^{i(\varphi_{ex}^{lx}+\delta_{ex}^{ly})} - e^{i(\varphi_{ey}^{ly}+\delta_{ey}^{lx})}) & e^{i(\varphi_{ex}^{lx}+\delta_{ex}^{ly})}\sin^2\Phi + e^{i(\varphi_{ey}^{ly}+\delta_{ey}^{lx})}\cos^2\Phi \end{bmatrix} \tag{4}$$

By combining eqs 2 and 4 the effect of LP cross-talk on the dual distorted phases $\varphi_1'(x, y)$ and $\varphi_2'(x, y)$ can be precisely evaluated. Moreover, it is evident that the phase distortions at CP states are proportional to the LP cross-talk measured by $\delta_{ex}^{ly}$ and $\delta_{ey}^{lx}$. Figure 1c shows how the perturbations $\delta_{ex}^{ly}$ and $\delta_{ey}^{lx}$ induced by the LP cross-talk feed back into the distortions of the ideal CP phases $\varphi_1(x, y)$ and $\varphi_2(x, y)$. As can be seen, the $\varphi_1'(x, y)$ and $\varphi_2'(x, y)$ obtained by the theory is highly related to the variations of $\delta_{ex}^{ly}$ and $\delta_{ey}^{lx}$ in the range of 60−180°, which a typical rectangular-patch meta-atom commonly exhibits (see Figure 2e). The phase tolerances measured by $\delta_1(x, y) = |\varphi'(x, y) - \varphi(x, y)|$ and $\delta_2(x, y) = |\varphi_2'(x, y) - \varphi_2(x, y)|$ vary between 0.1° and 137.9° and 0.6° and 178.9°. Such a level of phase distortion surely degrades significantly the resultant device's performance, such as low efficiency due to the emerging of undesired modes.[26] The above link established between the distortion of the CP phase profile and LP cross-talk affords us a guideline for precise dual-phase CP wavefront control. Therein, we can utilize the $\delta_{ex}^{ly}$ and $\delta_{ey}^{lx}$ obtained from full-wave finite-difference time domain (FDTD) calculations of a series of specific meta-atoms to evaluate the distortion of CP phases in practice. In what follows, we briefly introduce a procedure to design a type of meta-atom featuring extremely low LP cross-talk, which is particularly crucial for precisely realizing high-performance distinct bifunctionalities at two spin states.

**Meta-Atom and Metasurface Design.** To both achieve the large propagation phase cover and suppress the LP cross-talk, the meta-atom should exhibit multiple resonant modes while also a meandered fringe to avoid strong parallel capacitive coupling between adjacent elements. The designed basic building block is shown in Figure 2a. It consists of dual-layered identical composite metallic resonators and a back metallic ground plate. The interlayer coupling between the dual metallic patterns forms a Fabry−Perot resonance and thus enhances the phase accumulation. Two F4B dielectric boards each with $\varepsilon_r$ = 2.65, $h$ = 2.5 mm and a loss tangent of 0.001 are inserted between the resonators and the metallic square ground. Each composite resonator is specifically designed to contain both an inner cross patch and an external cross loop. These two structures exhibit at least two resonance modes, as evidenced by the two obvious dips in the reflection spectrum shown in Figure 2c. Notice that the couplings between different layers may split the two resonances into multiple modes at higher frequencies. Such a multiresonant behavior provides a great degree of freedom to engineer the phase slope and broaden the bandwidth. The key to avoid the LP cross-talk is to set the working frequency between the resonances of the dual or multiple operation modes, benefiting from the less-sensitive phase variation and the screening effect of the external loop, which enables the excited EM fields to be more strongly localized to the vicinities of the cross; see the right panel shown in Figure 2a. The physical insight for the screening effect is that $y$-directed currents along the edge of the $x$-oriented bar and loop are reversed and counteract the effect of $l_x$ variation, giving rise to the $l_x$-immune $\varphi_y$.

As shown in Figure 2b−d, the reflection magnitude of each meta-atom reaches near-unity ($|r| > 0.97$), while the reflection phase achieves a full 360° phase variation when $l_y$ varies within 0.5−3.45 mm. Most importantly, our meta-atom exhibits an extremely low LP cross-talk with $\delta_{ex}^{ly}$ or $\delta_{ey}^{lx}$ varying within 13.9−65° in the entire observed band of 9.5−11.5 GHz, which is in sharp contrast to 78−220° of the conventional rectangular-patch meta-atom, as shown in Figure 2e. This is especially evident at the target frequency of 10.5 GHz, where the LP cross-talk (15°) is an order of magnitude lower than that of rectangular-patch or elliptical-pillar meta-atoms (217°). Such a level of LP cross-talk only contributes to 7.5° distortion of $\varphi_1(x, y)$ and $\varphi_2(x, y)$, enabling a completely spin-decoupled feature and thus precise engineering of both the CP and LP phase profile. Moreover, it is important to note that the bandwidth with LP cross-talk less than 50° reaches 1.9 GHz. Here, the thickness of the dielectric board is selected as $h$ = 2.5 mm by taking a trade-off between the LP cross-talk, vertical profile, and the full phase cover. This is because the cross-talk slightly degrades, while in contrast the phase cover enhances as $h$ increases; see Figure S1 in the Supporting Information.

Given the merit of extremely low LP cross-talk of our meta-atom, the design of metasurfaces imposed by different combined phase profiles can be largely simplified. Therein, we only need one single parametric scanning of $ly$ to obtain the $\varphi \sim ly$ (the same with $\varphi \sim lx$ due to the 4-fold rotational symmetry) relation shown in Figure 2b by keeping $l_x$ = 2 mm ($l_y$ = 2) constant. Then, the required 2D phase distributions $\varphi_x(x, y)$, $\varphi_y(x, y)$ and metasurface layout can be exactly realized through a solution-finding algorithm according to $\varphi \sim ly$ ($\varphi \sim lx$). Otherwise, severe CP phase distortions will be induced by the aforementioned LP cross-talk when employing above process for design.

We next focus on the design of two metasurfaces manifesting distinct wavefronts. Both metadevices are designed to operate at $f_0$ = 10.5 GHz, and each consists of 27 × 27 anisotropic subwavelength meta-atoms, occupying a total size of $D \times D$ = 256.5 × 256.5 mm$^2$. The first metasurface (metadevice I) is designed to exhibit two functionalities: a linear phase profile for an oblique planar wavefront (anomalous reflection[27−35]) at the LCP state $\varphi_1(x, y) = \xi y$, with $\xi = 2\pi/L = 0.5k_0$ ($L$ = 57 mm being the super periodicity), and a spherical phase profile for focusing at the RCP state, with $\varphi_2(x, y) = \frac{2\pi}{\lambda}(\sqrt{x^2 + y^2 + F^2} - F)$ (with $F$ = 153.9 mm being the focal length and $\lambda$ the working wavelength). The second metasurface (metadevice II) generates a diffraction-free Bessel beam[36−41] for an incident LCP wave, with $\varphi_1(x, y) = \varphi_{\text{Axicon}} = \sin\left(\tan^{-1}\left(\frac{R}{F}\right)\right)\frac{2\pi}{\lambda}\sqrt{x^2 + y^2}$ ($F$ = 153.9 mm being the long depth of focus and $R$ half of the axicon aperture), a highly directive quad pencil beam at ($\varphi$ = 0°,

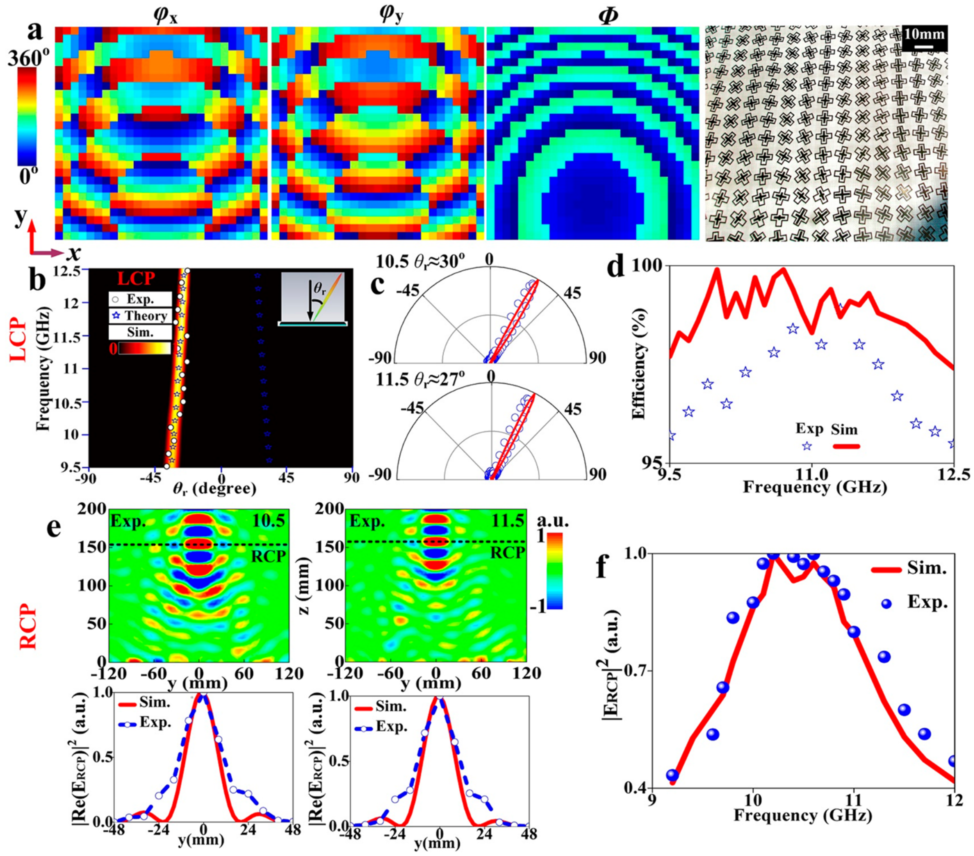

Figure 3. Characterization of the helicity-controlled bifunctional metadevice I in the (b−d) LCP and (e, f) RCP channel. (a) Calculated $\varphi_x$, $\varphi_y$, and $\Phi$ based on two input phase profiles shown in Figure 1c and the zoom-in-view photograph of the fabricated prototype. (b) Theoretical (blue stars) and FDTD-simulated and measured (circles) 2D contour of the far-field scattering power intensity $P(\theta_r, f)$ versus reflection angle/frequency and (c) far-field scattering patterns on the $yz$ plane at 10.5 and 11.5 GHz under plane LCP wave stimulation. (d) FDTD-simulated and measured efficiency calculated as the ratio between anomalously reflected power and the totally reflected power by integrating the scattered-field intensity within $-90° < \theta_r < 90°$ in steps of 1° (simulation) and 3° (measurement). (e) Measured Re($E_{RCP}$) field distributions (top panel) on the $yz$ plane and (bottom panel) along the focal lines at $z$ = 151/152 and 158/160 mm (simulation/measurement) at 10.5 and 11.5 GHz in steps of 2 and 8 mm. (f) Maximum $E$-field amplitude spectra at the focal point. Here, all fields are normalized against the peak value in the distributions.

90°, 180°, 270°; $\theta = 45°$) for an incident RCP wave with $\varphi_2(x, y) = \varphi_{\text{Quad-beam}}$ synthesized based on an alternating projection method (APM); see Figure S4a in the Supporting Information for the phase and APM details.

**Anomalous Reflection and Focusing.** We first characterize the anomalous reflection behavior of the metadevice I under LCP wave illumination. With the inputting linear and spherical phase profiles (Figure 1c), the final phases $\varphi_x$, $\varphi_y$, and $\Phi$ depicted in Figure 3a can be derived to map out the metadevice layout with spatially varying $l_x$ and $l_y$ and the orientation angles (see Figure S2a in the Supporting Information for more pixel-level details). Figure 3b depicts the theoretically calculated, FDTD-simulated and experimentally measured far-field scattering power intensity $P(\theta_r, \lambda)$ normalized to its maximum. As is shown, all results agree well, illustrating an obvious beam bending effect with reflection angle $\theta_r$ decreasing from 33.6° at 9.5 GHz to 24.9° at 12.5 GHz. Most importantly, the reflection beams contain only the desired anomalous mode with diffractions to the "wrong" channels fully suppressed. Such a pure-mode operation gives rise to the near 100% efficiency (defined as the ratio between anomalously reflected and totally reflected power) across a broadband spectrum (~97.4/95.7 in simulation/measurement) shown in Figure 3d, which is highly superior to available microwave metasurfaces launched by LP or CP waves. The absolute efficiency regarding the cross-polarization components (defined as the ratio between anomalously reflected power and total incident power) still reaches ~90.7%; see Figure S2b in the Supporting Information. This superior performance can be attributed to two factors: dispersionless PB phase and meta-atoms with low LP cross-talk. The high-efficiency anomalous reflection can be further inspected from the measured scattering patterns at 10.5 and 11.5 GHz shown in Figure 3c, where the FDTD simulations again match very well with the experimental data.

We next move to the other functionality of our metadevice at the RCP wave. Figure 3e displays the measured Re($E_{RCP}$) distributions of the reflected beam on $yz$ planes (top panel) and along the focal lines (bottom panel) at 10.5 and 11.5 GHz, showing clearly that the incoming plane wave has been converged to a point near $F$ = 150 mm. As expected, the field distribution Re($E_{RCP}$) along the focal lines reaches a maximum at the expected focal points in the above two particular cases studied. The simulated/measured focal-spot size characterized by the half power beamwidth (HPBW) is obtained as 21/23 mm at 10 GHz and 19/20 mm at 11.5 GHz, which is very close to the theoretical limitation of 19.5 and 17 mm determined by aperture size and focal length. Finally, we show in Figure 3f the simulated and measured maximum $E$-field amplitude spectra at the focal point to quantitatively evaluate the working bandwidth. As expected, the $E$-field intensity is almost at its maximum around



DOI: 10.1021/acsphotonics.8b01439
ACS Photonics 2019, 6, 211−220

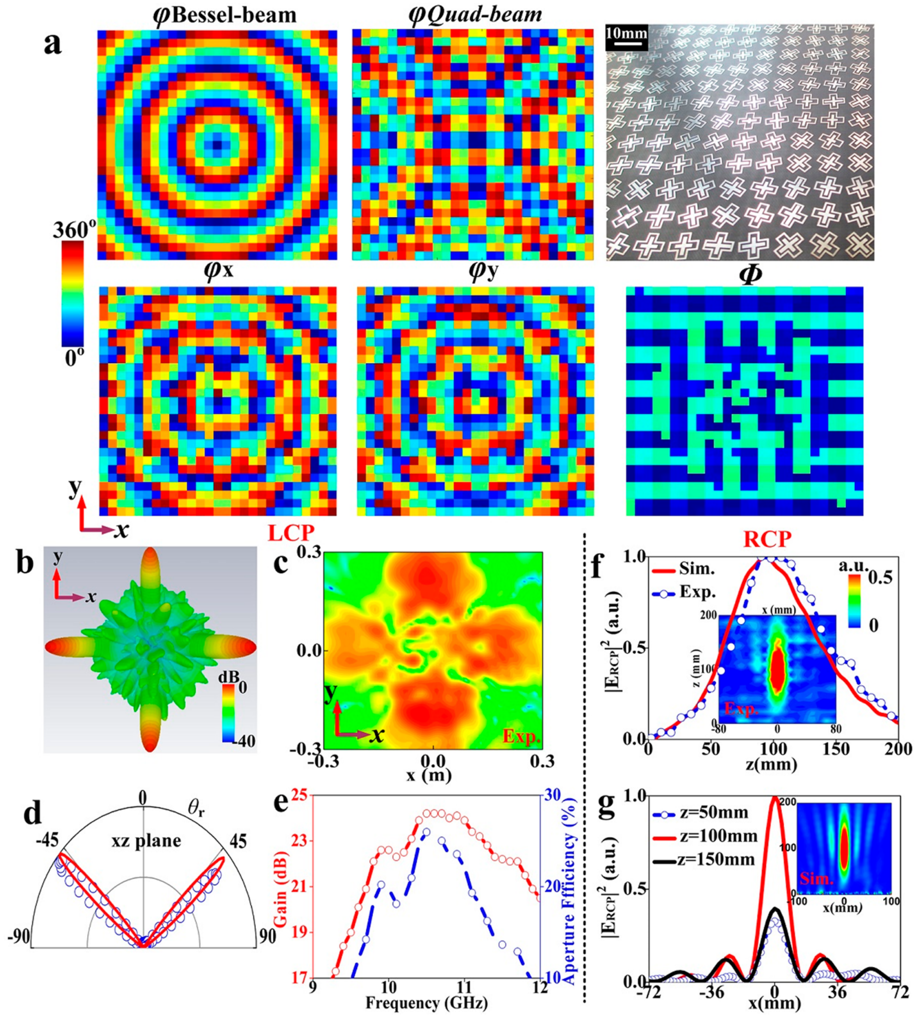


**Figure 4.** Characterization of the helicity-controlled bifunctional metadevice II in (b−e) LCP and (f, g) RCP channels at 10.5 GHz. (a) Calculated $\varphi_x$, $\varphi_y$, and $\Phi$ (bottom row) based on two CP phase profiles of $\varphi_1(x, y) = \varphi_{\text{Bessel-beam}}$ and $\varphi_2(x, y) = \varphi_{\text{Quad-beam}}$ (top row) and zoom-in-view fabricated prototype. (b) FDTD-simulated snapshots of the 3D far-field radiation patterns. (c) Measured near-field distribution and (d) 2D radiation patterns on the $xz$ plane. (e) Measured gain and aperture efficiency. In (b)−(e), the results are achieved by feeding the metasurface with a small LCP horn. (f) Comparison of simulated and measured field intensity along the propagating direction ($z$ axis) at $x = 0$ mm. (g) FDTD-calculated field intensity at various $xz$ planes of $z = 50$, 100, and 150 mm away from the metadevice. The insets to (f) and (g) depict the measured and simulated field-intensity on the $xz$ plane ($y = 0$ mm), respectively. In (f) and (g), the results are obtained by normally shining the metasurface with a plane RCP wave. All fields have been normalized against their peak value.

the target frequency $f_0 = 10.5$ GHz, indicating the best focusing performance. However, the focusing performance deteriorates as frequencies go beyond the target one since the phase profile no longer strictly follows the required dispersive spherical phase $\varphi_2(x, y)$. The working bandwidth measured by the HPBW is about 2.2 GHz (9.4−11.6 GHz), within which slight fluctuations of maximum $E$-field intensity are observed with shallow dips induced by the amplitude fluctuations of the meta-atoms at different frequencies. The working efficiency, defined as the ratio between the powers carried by the focal spot and the incident beam, is obtained in the range of 90.2−92.7%. The slight deviation between the measured and designed values can be attributed to the tolerances inherent in sample fabrication and measurements, especially for the imperfect nonplanar incoming wavefront. More detailed information on how to identify the focal spot and the focusing behavior on the $xz$ plane and at other frequencies can be found in Figure S3 in the Supporting Information.

**Quad-Beam and Bessel Beam Generation.** In this subsection, we will further demonstrate the possible applications of our metasurface by numerically and experimentally investigating the performance of bifunctional metadevice II. Using the same method as metadevice I, $\varphi_x$, $\varphi_y$, and $\Phi$ (bottom row of Figure 4a) of metadevice II can be derived from two CP phase profiles of $\varphi_1(x, y) = \varphi_{\text{Bessel-beam}}$ and $\varphi_2(x, y) = \varphi_{\text{Quad-beam}}$ (top row) to map out the metadevice layout (Figure 4a and Figure S4b in the Supporting Information). Figure 4b shows snapshots of 3D far-field radiation patterns at four representative frequencies when metadevice II is fed by a LCP horn antenna placed at $F = 153.9$ mm. Four quasi-symmetric highly directive pencil beams are clearly observed in all cases studied, coinciding well the theoretically calculated patterns shown in Figure S3a. The physics for the quad-beam emissions lies in the efficiently formed four spots with highly localized fields, as confirmed by the measured field map shown in Figure 4c. As depicted in Figure 4d, the simulated/measured HBPW of a typical beam is calculated as ∼9/10.5° and the backlobes are significantly lower,


DOI: 10.1021/acsphotonics.8b01439
ACS Photonics 2019, 6, 211−220

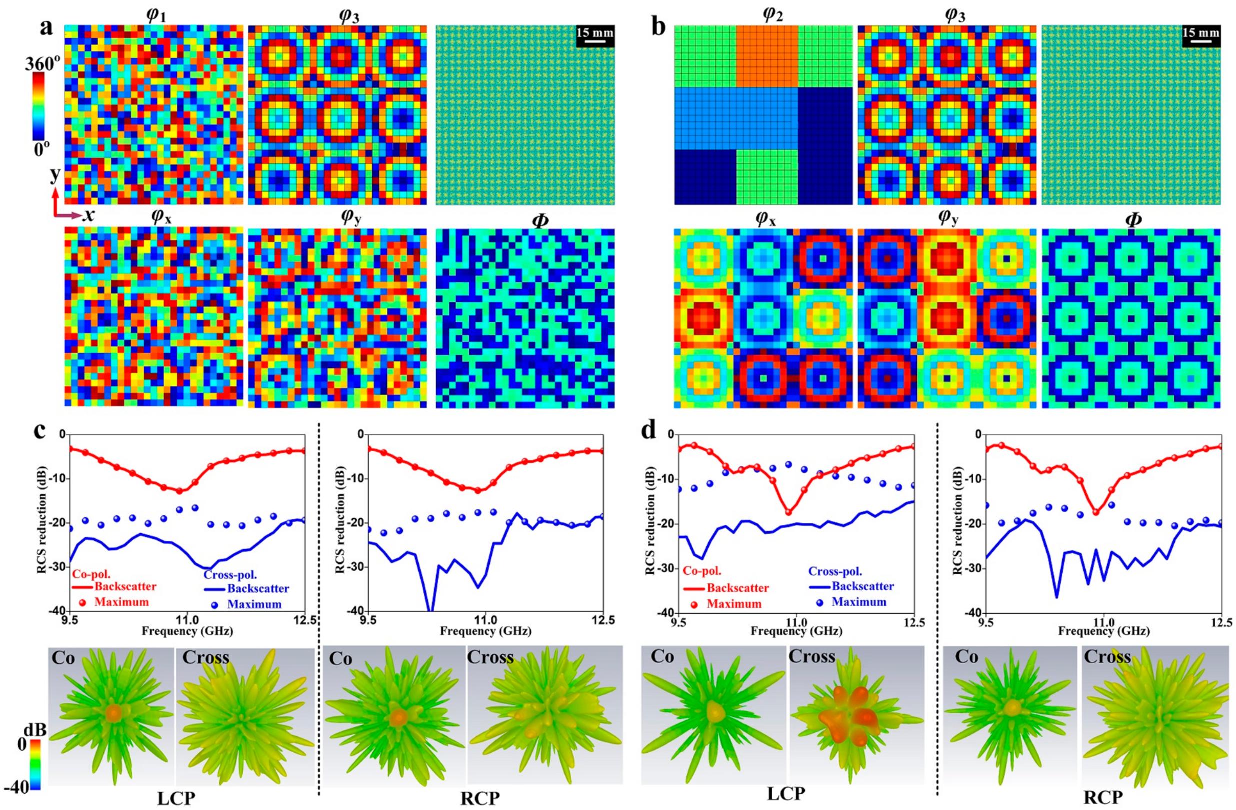


**Figure 5.** Illustration of possible applications by examining versatile scattering patterns imposed on two spin-decoupled helicity channels of our (a, c) hybrid random-spherical and (b, d) hybrid uniform-spherical phased metasurfaces composed of 27 × 27 meta-atoms. (a, b) Calculated $\varphi_x$, $\varphi_y$, and Φ (bottom row) based on two CP phase profiles (top row) and corresponding metasurface layouts. (c, d) FDTD-calculated RCS reduction spectrum at the normal and maximum direction (top row) and far-field scattering patterns (bottom row) at 10.5 GHz under LCP and RCP channels. Here, the phase in the random case has a completely stochastic global profile in the range of 0−360°, whereas in the latter two cases it exhibits a local uniform or spherical profile for each subarray of 9 × 9 meta-atoms, while additional global profile for 3 × 3 subarrays through arbitrary digital sequences. In the current design, all utilized global sequences are [2, 3, 2; 1, 1, 0; 0, 2, 0], with 0, 1, 2, and 3 corresponding to 00, 01, 10, and 11 states of a typical 2-bit coding and phases of 0°, 90°, 180°, and 270°.

below −20/−15 dB, at most elevation angles. As shown in Figure 4e, the peak gain and aperture efficiency are measured as 24.2 dB and 26% at 10.5 GHz, and the working bandwidth measured by ±1 dB gain variation reaches 1.8 GHz (17%). The slightly asymmetric patterns with small intensity deviations observed among the four beams at different frequencies are partially originated from the slightly asymmetric phase profile $\varphi_2(x, y) = \varphi_{\text{Quad-beam}}$ optimized based on APM and are partially attributable to the asymmetric patterns of the utilized feed source.

Finally, we evaluate the performance of nondiffracting axicon lenses triggered by a normally incident plane RCP wave. Figure 4f compares the simulated and measured field intensities along the propagation direction ($z$ axis) at $x = 0$ mm, while Figure 4g presents the FDTD-calculated field intensity on three $xz$ planes of $z$ = 50, 100, and 150 mm away from the metadevice. The insets depict the measured and FDTD-simulated field intensity distributions, where a reasonable consistency is observed. As shown in Figure 4f, the energy is mainly confined around the optical axis and propagates along the axis over a considerable distance (approximate to 100 mm measured by 3 dB energy attenuation) without diffraction. The beamwidths for the Bessel beams are about 14 mm at its half power decay and remain almost constant as frequency varies, as shown by Figure 4g, where good Bessel-like profiles of electric fields with first zero are clearly observed. More information about the interpretation of the data and results on other planes and at other frequencies can be found in Figures S5 and S6 in the Supporting Information.

**Versatile Scattering Patterns for Different Applications.** Our completely decoupled hybrid strategy can find many other interesting applications, which will be briefly introduced in this section. In previous discussions, we have successfully demonstrated the potential applications of our proposal in a regular manner, where the phase distributions are all gradually changed. Here, we verify that our strategy can be also efficiently adopted in a more general scenario, where abrupt phase changes or even irregular phase distributions are required. The basic purpose targeted here is to generate two versatile diffusive scattering patterns for monostatic/bistatic radar cross section (RCS) reduction[42] or multichannel communications and multitarget radars in terms of information entropy[43] under two orthogonal CP channels by taking advantage of completely spin-decoupled feature.

Two design examples are given by merging two of three different irregular phase patterns $\varphi_1$, $\varphi_2$, and $\varphi_3$ shown in Figure 5a and b: the hybrid random-spherical and the hybrid uniform-spherical phased metasurfaces each composed of 27 × 27 meta-atoms. Therein, the phase in the random case has a completely global stochastic profile in the range 0−360°, whereas in the latter two cases it contains a local uniform or spherical profile in 9 × 9 meta-atoms of a subarray, while additional global profile $\varphi_0(\xi) = 2\pi\xi/2^{\sigma}$ ($\sigma$ = 1, 2, 3, ... is the bit and $\xi$ describes different


DOI: 10.1021/acsphotonics.8b01439
ACS Photonics 2019, 6, 211−220

states) for 3 × 3 subarrays through arbitrary digital $\sigma$-bit sequences. Taking a 2-bit design in the current work for example, the global profile is 0°, 90°, 180°, and 270° at four digital states of $\xi = 0$ (00), 1 (01), 2 (10), and 3 (11). Here, the focal length of the spherical subarray is designed as $F = 12$ mm such that the spherical phase $\varphi(x, y) = \frac{2\pi}{\lambda}(\sqrt{x^2 + y^2 + F^2} - F)$ covers a full $2\pi$, and all global sequences utilized are [2, 3, 2; 1, 1, 0; 0, 2, 0].

The performances of both hybrid random-spherical and uniform-spherical phased metasurfaces are numerically characterized through FDTD calculations by illuminating them with a normally incident plane CP wave. As shown in Figure 5c and d, the copolarized components exhibit almost the same backscattering behavior with the peak intensity occurring at the normal under LCP and RCP channels. This is quite physical because they do not carry any PB phase information and thus are unable to see the desired phase profile. The copolarized RCS reduction is obtained due to the significantly suppressed scattering intensity of each pixel, which alters as orientations and structures vary. However, the case is completely different for the cross-polarized components which are strongly insensitive to the individually imposed phase patterns. For example, the digital spherical-phase profile always manifests a desirable diffusive pattern with extremely low peak and backscattered RCS (more than −15.7 dB relative to the RCS of the same-sized metallic ground) across the entire band. In contrast, the digital uniform-phase profile exhibits strong scatterings at a certain direction with a peak value of −6.7 dB. Although the random-phase profile here achieves a desirable diffusion behavior, it is optimized and does not always hold. The almost identical scattering feature of the two metasurfaces under the RCP channel further verifies the complete decoupling of the dual-channel CP phases. Besides the RCS reduction for stealth applications, the large physical entropy determined by the innumerable scattering beams of the far-field patterns enhances considerably the information capacity. As a consequence, the dual decoupled channels with individually imposed phase patterns are very beneficial for radar, imaging, and communications from the perspective of information Shannon entropy.

## ■ DISCUSSION

To sum up, we have demonstrated independent wavefront control that can be individually modulated by imposing both the geometric and propagation phases of inhomogeneous and anisotropic metasurfaces. By utilizing the meta-atoms with low LP cross-talk, CP multifunctionalities and extreme wavefront controls can be merged into a single flat device with high working efficiency. For verification, two bifunctional metadevices with a thin thickness of $\lambda/6$ have been designed, and numerically and experimentally characterized. Both devices exhibit desirable wavefront control and elegant performances with a high efficiency over 90%. It should be strongly mentioned that the LP cross-talk cannot be an issue if we utilize the 2D phase relation $\varphi \approx (lx, ly)$ subjected to double parametric scanning of $lx$ and $ly$. However, this prohibitively enhances the computation volume (exponential growth) and complicates the design; for example, a typical 80-step single parametric scanning will lead to 6400 calculations for a double scanning. This is even impossible for the design of a large array with broad phase cover. Moreover, there may be even no such solution that simultaneously fulfills $\varphi_x$ and $\varphi_y$ at certain position. Therefore, the double-scanning approach is only applicable from a theoretical perspective and thus is beyond the scope of this work. Our method can also be applied to designing more complex wavefronts and functionalities by superimposing several different phase profiles[13,14,44−48] in each helicity channel, facilitating helicity-multiplexed multifunctional metadevices. Moreover, it is also readily extended to optical frequencies by using a single-layered composite metallic pattern based on electron beam lithography and also to a transmissive scheme by replacing the background with an identical metallic pattern; see Figure S7 in the Supporting Information. Our finding opens an avenue for complex CP wavefront control with high integrity and fidelity and low cost.

## ■ METHODS

**Numerical Characterizations.** All numerical designs and characterizations are performed through FDTD simulations based on a commercial software package. Specifically, the reflection amplitudes/phases are obtained by studying a single meta-atom with periodic conditions imposed at its four boundaries and a Floquet port assigned at a distance of 15 mm away from the $xy$-plane where the meta-atom is placed. In the far-field and near-field calculations, we characterized the entire metasurfaces each consisting of 27 × 27 meta-atoms, with open boundary conditions set at its four boundaries in the $xy$-plane. In all cases, the metasurface/meta-atom is illuminated by normally incident LCP and RCP plane waves.

**Fabrications and Experiments.** The dual-layer metallic patterns of each metadevice are fabricated on two dielectric boards using a printed-circuit-board (PCB) technique. They are aligned with each other through several embedded vias, assembled together through adhesives, and finally reinforced through a hot press. The experimental near-field or far-field characterizations of all samples are performed in a microwave anechoic chamber using an angle-resolved experimental setup; see Figure S8 in the Supporting Information. In anomalous-reflection measurements, two CP horns, exhibiting a voltage standing wave ratio less than 2.5 and an axial ratio less than 3.5 dB within 6−18 GHz, are adopted as the receiver and transmitter and placed 1 m away from the sample. The receiving CP horn, which was aligned with the metasurface, rotated freely and recorded the signal scattered within $-90° < \theta_r < 90°$. In radiation pattern measurements, the metasurface was fed by a small CP horn at the focal point, and both of them were fixed on a big foam, which can be rotated freely along the foam's axial center. The receiving CP horn was placed 10 m away to record the far-field signals. In near-field measurements, the metasurface and launched CP horn were fixed with a distance of 0.8 m to guarantee a plane wave excitation, where the spot size of the emitted beam is obtained larger than two-thirds of the sample aperture at the sample plane. A 15 mm-long monopole antenna was placed between them and fixed to a 2D electronic step motor that can move automatically in a maximum area of 0.6 m × 0.6 m with a step resolution of 8 mm. The measured LCP and RCP components can be calculated as $E_{\mathrm{LCP}} = \frac{1}{\sqrt{2}}(E_x - iE_y)$ and $E_{\mathrm{LCP}} = \frac{1}{\sqrt{2}}(E_x + iE_y)$, by incorporating both measured $E_x$ and $E_y$ fields through a monopole. In the near-field characterizations, the required reflected wave components are obtained by purposely deducting the fields recorded in free space (without metasurface) from the total signal fields measured when the metasurface is available.



DOI: 10.1021/acsphotonics.8b01439
ACS Photonics 2019, 6, 211−220

## ASSOCIATED CONTENT

### Supporting Information

The Supporting Information is available free of charge on the ACS Publications website at DOI: 10.1021/acsphotonics.8b01439.

(Additional theory for spin-decoupled phase control; the effect of $h$ on the cross-talk and phase cover; additional information for bifunctional metadevice I studied in Figure 3; additional information for bifunctional metadevice II studied in Figure 4; extension of the spin-decoupled strategy to a transmission scheme; experimental setup PDF)

## AUTHOR INFORMATION


### Corresponding Authors

*H.-X. Xu, E-mail: hxxuellen@gmail.com.
* C.-W. Qiu, E-mail: eleqc@nus.edu.sg.

### ORCID

He-Xiu Xu: 0000-0003-0156-7642
Shuang Zhang: 0000-0003-4556-2333
Cheng-Wei Qiu: 0000-0002-6605-500X


### Author Contributions

#H.-X. Xu and L. Han contributed equally to this work.

### Notes

The authors declare no competing financial interest.

## ACKNOWLEDGMENTS

This work was supported by National Natural Science Foundation of China (NSFC) (61501499, 11634010); National Defense Foundation of China (2201078); Key Program of National Natural Science Foundation of Shaanxi Province (2017KJXX-24); Youth Talent Lifting Project of the China Association for Science and Technology (17-JCJQ-QT-003); China Scholarship Fund (CSC) (201703170022 and 201706290164); and also Aviation Science Foundation of China (20161996009). C.W.Q. acknowledges the financial support from the National Research Foundation, Prime Minister's Office, Singapore, under its Competitive Research Program (CRP award NRF-CRP15-2015-03).

## REFERENCES


(1) Kats, M. A.; Genevet, P.; Aoust, G.; Yu, N.; Blanchard, R.; Aieta, F.; Gaburro, Z.; Capasso, F. Giant birefringence in optical antenna arrays with widely tailorable optical anisotropy. *Proc. Natl. Acad. Sci. U. S. A.* **2012**, *109*, 12364−12368.

(2) Pors, A.; Albrektsen, O.; Radko, I. P.; Bozhevolnyi, S. I. Gap plasmon-based metasurfaces for total control of reflected light. *Sci. Rep.* **2013**, *3*, 2155.

(3) Chen, W. T.; Yang, K. Y.; Wang, C. M.; Huang, Y. W.; Sun, G.; Chiang, I. D.; Liao, C. Y.; Hsu, W. L.; Lin, H. T.; Sun, S.; Zhou, L. High-efficiency broadband meta-hologram with polarization-controlled dual images. *Nano Lett.* **2014**, *14*, 225−230.

(4) Jia, S. L.; Wan, X.; Bao, D.; Zhao, Y. J.; Cui, T. J. Independent controls of orthogonally polarized transmitted waves using a Huygens metasurface. *Laser Photonics Rev.* **2015**, *9*, 545−553.

(5) Ma, H. F.; Wang, G. Z.; Kong, G. S.; Cui, T. J. Independent controls of differently-polarized reflected waves by anisotropic metasurfaces. *Sci. Rep.* **2015**, *5*, 9605.

(6) Huang, Y. W.; Chen, W. T.; Tsai, W. Y.; Wu, P. C.; Wang, C. M.; Sun, G.; Tsai, D. P. Aluminum plasmonic multicolor meta-hologram. *Nano Lett.* **2015**, *15*, 3122−3127.

(7) Liu, S.; Cui, T. J.; Xu, Q.; Bao, D.; Du, L.; Wan, X.; Tang, W. X.; Ouyang, C.; Zhou, X. Y.; Yuan, H.; Ma, H. F. *Light: Sci. Appl.* **2016**, *5*, No. e16076.

(8) Xu, H. X.; Tang, S.; Ling, X.; Luo, W.; Zhou, L. Flexible control of highly-directive emissions based on bifunctional metasurfaces with low polarization cross-talking. *Ann. Phys.* **2017**, *529*, 201700045.

(9) Cai, T.; Wang, G.; Tang, S.; Xu, H. X.; Duan, J.; Guo, H.; Guan, F.; Sun, S.; He, Q.; Zhou, L. High-efficiency and full-space manipulation of electromagnetic wave fronts with metasurfaces. *Phys. Rev. Appl.* **2017**, *8*, No. 034033.

(10) Xu, H. X.; Zhang, L.; Kim, Y.; Wang, G. M.; Zhang, X. K.; Sun, Y.; Ling, X.; Liu, H.; Chen, Z.; Qiu, C. W. Wavenumber-splitting metasurfaces achieve multi-channel diffusive invisibility. *Adv. Opt. Mater.* **2018**, *6*, 1800010.

(11) Chen, X.; Huang, L.; Mühlenbernd, H.; Li, G.; Bai, B.; Tan, Q.; Jin, G.; Qiu, C. W.; Zhang, S.; Zentgraf, T. Dual-polarity plasmonic metalens for visible light. *Nat. Commun.* **2012**, *3*, 1198.

(12) Ding, X.; Monticone, F.; Zhang, K.; Zhang, L.; Gao, D.; Burokur, S. N.; Lustrac, A. de; Wu, Q.; Qiu, C. W.; Alù, A. Ultrathin pancharatnam-berry metasurface with maximal cross-polarization efficiency. *Adv. Mater.* **2015**, *27*, 1195−1200.

(13) Mei, S.; Mehmood, M. Q.; Hussain, S.; Huang, K.; Ling, X.; Siew, S. Y.; Liu, H.; Teng, J.; Danner, A.; Qiu, C. W. Flat helical nanosieves. *Adv. Funct. Mater.* **2016**, *26*, 5255−5262.

(14) Mehmood, M. Q.; Mei, S.; Hussain, S.; Huang, K.; Siew, S. Y.; Zhang, L.; Zhang, T.; Ling, X.; Liu, H.; Teng, J.; Danner, A. Visible-frequency metasurface for structuring and spatially multiplexing optical vortices. *Adv. Mater.* **2016**, *28*, 2533−2539.

(15) Wang, S.; Wu, P. C.; Su, V. C.; Lai, Y. C.; Chu, C. H.; Chen, J. W.; Lu, S. H.; Chen, J.; Xu, B.; Kuan, C. H.; Li, T. Broadband achromatic optical metasurface devices. *Nat. Commun.* **2017**, *8*, 187.

(16) Wen, D.; Yue, F.; Li, G.; Zheng, G.; Chan, K.; Chen, S.; Chen, M.; Li, K. F.; Wong, P. W. H. K.; Cheah, W.; Pun, E. Y. B. Helicity multiplexed broadband metasurface holograms. *Nat. Commun.* **2015**, *6*, 8241.

(17) Wen, D.; Chen, S.; Yue, F.; Chan, K.; Chen, M.; Ardron, M.; Li, K. F.; Wong, P. W. H.; Cheah, K. W.; Pun, E. Y. B.; Li, G. Metasurface device with helicity-dependent functionality. *Adv. Opt. Mater.* **2016**, *4*, 321−327.

(18) Zhang, F.; Pu, M.; Li, X.; Gao, P.; Ma, X.; Luo, J.; Yu, H.; Luo, X. All-dielectric metasurfaces for simultaneous giant circular asymmetric transmission and wavefront shaping based on asymmetric photonic spin-orbit interactions. *Adv. Funct. Mater.* **2017**, *27*, 1704295.

(19) Kamalia, S. M.; Arbabia, E.; Arbabi, A.; Faraon, A. A review of dielectric optical metasurfaces for wavefront control. *Nanophotonics* **2018**, *7*, 1041−1068.

(20) Liu, Y.; Ke, Y.; Luo, H.; Wen, S. Photonic spin Hall effect in metasurfaces: a brief review. *Nanophotonics* **2017**, *6*, 51−70.

(21) Chen, H.-T.; Taylor, A. J.; Yu, N. A review of metasurfaces: physics and applications. *Rep. Prog. Phys.* **2017**, *79*, No. 076401.

(22) Zhang, X.; Pu, M.; Jin, J.; Li, X.; Gao, P.; Ma, X.; Wang, C.; Luo, X. Helicity multiplexed spin-orbit interaction in metasurface for colorized and encrypted holographic display. *Ann. Phys.* **2017**, *529*, 1700248.

(23) Arbabi, A.; Horie, Y.; Bagheri, M.; Faraon, A. Dielectric metasurfaces for complete control of phase and polarization with subwavelength spatial resolution and high transmission. *Nat. Nanotechnol.* **2015**, *10*, 937.

(24) Mueller, J. P. B.; Rubin, N. A.; Devlin, R. C.; Groever, B.; Capasso, F. Metasurface polarization optics: independent phase control of arbitrary orthogonal states of polarization. *Phys. Rev. Lett.* **2017**, *118*, 113901.

(25) Devlin, R. C.; Ambrosio, A.; Rubin, N. A.; Mueller, J. P. B.; Capasso, F. Arbitrary spin-to−orbital angular momentum conversion of light. *Science* **2018**, *358*, 896−901.

(26) Xu, H. X.; Tang, S.; Ma, S.; Luo, W.; Cai, T.; Sun, S.; He, Q.; Zhou, L. Tunable microwave metasurfaces for high-performance operations: dispersion compensation and dynamical switch. *Sci. Rep.* **2016**, *6*, 38255.

(27) Yu, N.; Genevet, P.; Kats, M. A.; Aieta, F.; Tetienne, J. P.; Capasso, F.; Gaburro, Z. Light propagation with phase discontinuities: generalized laws of reflection and refraction. *Science* **2011**, *334*, 333–337.
(28) Ni, X.; Emani, N. K.; Kildishev, A.; Boltasseva, A.; Shalaev, V. M. Broadband light bending with plasmonic nanoantennas. *Science* **2012**, *335*, 427.
(29) Sun, S.; Yang, K. Y.; Wang, C. M.; Juan, T. K.; Chen, W. T.; Liao, C. Y.; He, Q.; Xiao, S.; Kung, W. T.; Guo, G. Y.; Zhou, L. High-efficiency broadband anomalous reflection by gradient meta-surfaces. *Nano Lett.* **2012**, *12*, 6223–6229.
(30) Li, Z.; Palacios, E.; Butun, S.; Aydin, K. Visible-frequency metasurfaces for broadband anomalous reflection and high-efficiency spectrum splitting. *Nano Lett.* **2015**, *15*, 1615–1621.
(31) Zhang, X.; Tian, Z.; Yue, W.; Gu, J.; Zhang, S.; Han, J.; Zhang, W. Broadband terahertz wave deflection based on c-shape complex metamaterials with phase discontinuities. *Adv. Mater.* **2013**, *25*, 4567–4572.
(32) Pfeiffer, C.; Emani, N. K.; Shaltout, A. M.; Boltasseva, A.; Shalaev, V. M.; Grbic, A. Efficient light bending with isotropic metamaterial Huygens' surfaces. *Nano Lett.* **2014**, *14*, 2491–2497.
(33) Liu, L.; Zhang, X.; Kenney, M.; Su, X.; Xu, N.; Ouyang, C.; Shi, Y.; Han, J.; Zhang, W.; Zhang, S. Broadband metasurfaces with simultaneous control of phase and amplitude. *Adv. Mater.* **2014**, *26*, 5031–5036.
(34) Aieta, F.; Kats, M. A.; Genevet, P.; Capasso, F. Multiwavelength achromatic metasurfaces by dispersive phase compensation. *Science* **2015**, *347*, 1342–1345.
(35) Liu, Z.; Li, Z.; Liu, Z.; Li, J.; Cheng, H.; Yu, P.; Liu, W.; Tang, C.; Gu, C.; Li, J.; Chen, S. High-performance broadband circularly polarized beam deflector by mirror effect of multi-nano-rod metasurfaces. *Adv. Funct. Mater.* **2015**, *25*, 5428–5434.
(36) Durnin, J.; Miceli, J. J.; Eberly, J. H. Diffraction-free beams. *Phys. Rev. Lett.* **1987**, *58*, 1499–1501.
(37) Qi, M. Q.; Tang, W. X.; Cui, T. J. A broadband bessel beam launcher using metamaterial lens. *Sci. Rep.* **2014**, *5*, 11732.
(38) Li, Y. B.; Cai, B. G.; Wan, X.; Cui, T. J. Diffraction-free surface waves by metasurfaces. *Opt. Lett.* **2014**, *39*, 5888–5891.
(39) Pfeiffer, C.; Grbic, A. Controlling vector Bessel beams with metasurfaces. *Phys. Rev. Appl.* **2014**, *2*, No. 044012.
(40) Aieta, F.; Genevet, P.; Kats, M. A.; Yu, N.; Blanchard, R.; Gaburro, Z.; Capasso, F. Aberration-free ultrathin flat lenses and axicons at telecom wavelengths based on plasmonic metasurfaces. *Nano Lett.* **2012**, *12*, 4932–4936.
(41) Chen, W. T.; Khorasaninejad, M.; Zhu, A. Y.; Oh, J.; Devlin, R. C.; Zaidi, A.; Capasso, F. Generation of wavelength-independent subwavelength Bessel beams using metasurfaces. *Light: Sci. Appl.* **2016**, *6*, No. e16259.
(42) Maguid, E.; Yulevich, I.; Veksler, D.; Kleiner, V.; Brongersma, M. L.; Hasman, E. Photonic spin-controlled multifunctional shared-aperture antenna array. *Science* **2016**, *352*, 1202–1206.
(43) Liu, S.; Cui, T. J.; Zhang, L.; Xu, Q.; Wang, Q.; Wan, X.; Gu, J. Q.; Tang, W. X.; Qi, M. Q.; Han, J. G.; Zhang, W. L. Convolution operations on coding metasurface to reach flexible and continuous controls of terahertz beams. *Adv. Sci.* **2016**, *3*, 1600156.
(44) Ma, X.; Pu, M.; Li, X.; Huang, C.; Wang, Y.; Pan, W. A planar chiral meta-surface for optical vortex generation and focusing. *Sci. Rep.* **2016**, *5*, 10365.
(45) Zhang, L.; Liu, S.; Li, L.; Cui, T. J. Spin-controlled multiple pencil beams and vortex beams with different polarizations generated by Pancharatnam-Berry coding metasurfaces. *ACS Appl. Mater. Interfaces* **2017**, *9*, 36447–36455.
(46) Kamali, S. M.; Arbabi, E.; Arbabi, A.; Horie, Y.; Faraji-Dana, M.; Faraon, A. Angle-multiplexed metasurfaces: encoding independent wavefronts in a single metasurface under different illumination angles. *Phys. Rev. X* **2017**, *7*, No. 041056.
(47) Xu, H. X.; Ma, S.; Ling, X.; Zhang, X. K.; Tang, S.; Cai, T.; Sun, S.; He, Q.; Zhou, L. Wavenumber-splitting metasurfaces achieve multi-channel diffusive invisibility. Deterministic approach to achieve broadband polarization-independent diffusive scatterings based on metasurfaces. *ACS Photonics* **2018**, *5*, 1691–1702.
(48) Cui, T.-J.; Liu, S.; Li, L.-L. Information entropy of coding metasurface. *Light: Sci. Appl.* **2016**, *5*, e16172.



DOI: 10.1021/acsphotonics.8b01439
*ACS Photonics* 2019, 6, 211–220